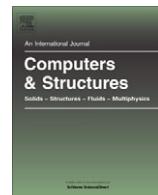




Contents lists available at SciVerse ScienceDirect

## Computers and Structures

journal homepage: [www.elsevier.com/locate/compstruc](http://www.elsevier.com/locate/compstruc)

# Two-dimensional simulation of the fluttering instability using a pseudospectral method with volume penalization

Thomas Engels <sup>a,b,\*</sup>, Dmitry Kolomenskiy <sup>c</sup>, Kai Schneider <sup>a</sup>, Jörn Sesterhenn <sup>b</sup><sup>a</sup> Laboratoire de Mécanique, Modélisation et Procédés Propres (M2P2), CNRS et Aix-Marseille Université, France<sup>b</sup> Institut für Strömungsmechanik und Technische Akustik (ISTA), TU Berlin, Germany<sup>c</sup> McGill University/CRM, Montréal, Canada

## ARTICLE INFO

## Article history:

Received 31 May 2012

Accepted 4 December 2012

Available online xxxx

## Keywords:

Fluid–structure interaction

Fluttering instability

Volume-penalization method

Spectral method

## ABSTRACT

We present a new numerical scheme for the simulation of deformable objects immersed in a viscous incompressible fluid. The two-dimensional Navier–Stokes equations are discretized with an efficient Fourier pseudo-spectral scheme. Using the volume penalization method arbitrary inflow conditions can be enforced, together with the no-slip conditions at the boundary of the immersed flexible object. With respect to Kolomenskiy and Schneider (2009) [1], where rigid moving obstacles have been considered, the present work extends the volume penalization method to account for moving deformable objects while avoiding numerical oscillations in the hydrodynamic forces. For the solid part, a simple and accurate one-dimensional model, the non-linear beam equation, is employed. The coupling between the fluid and solid parts is realized with a fast explicit staggered scheme. The method is applied to the fluttering instability of a slender structure immersed in a free stream. This coupled non-linear system can enter three distinct states: stability of the initial condition or maintenance of an either periodic or chaotic fluttering motion. We present a detailed parameter study for different Reynolds numbers and reduced free-stream velocities. The dynamics of the transition from a periodic to a chaotic state is investigated. The results are compared with those obtained by an inviscid vortex shedding method [2] and by a viscous linear stability analysis [3], yielding for both satisfactory agreement. New results concerning the transition to chaos are presented.

© 2012 Elsevier Ltd. All rights reserved.

## 1. Introduction

In nature inspired fluid dynamics, the complex interaction of some deformable structures with an ambient flow is a commonplace problem. Whether it is gliding, swimming or flying, many types of animal locomotion strongly rely on this type of interaction [4]. The archetype problem of fluid–structure interaction is the flapping of a flag in the wind, attracting researchers due to its richness in phenomena. Indeed, a flag exhibits a large variety of possible regimes, depending on its material parameters and the surrounding flow. It can be aligned with the flow in a stable state, or flap dynamically. The latter state can further be subdivided into highly regular and chaotic motion patterns. In some parameter ranges, also bistable behavior has been reported, where the dynamically selected state depends on the initial conditions.

Natural swimmers and flapping flyers exploit a combination of active and passive flapping to improve their flight performance

[5–7], a source of inspiration for various investigations. Also, aside from locomotion, the fluttering instability occurs in other biological applications. Huang [8] first pointed out that flutter is encountered in the upper human airways, where the soft palate separates nasal and oral inflow. The instability manifests itself in the occurrence of snoring or, in severe cases, obstructive sleep apnoea/hypopnea.

In engineering, the flutter phenomenon occurs as a problem in printing machines, where flutter limits the speed for moving sheets [9]. However, it is not only destructive and perturbing if flutter occurs in technical applications. The concept of a flutter-mill, a small scale device for energy harvesting, is based on the fact that if the instability threshold is exceeded, energy is pumped continuously into the structure. This energy, originating from the mean flow, can partly be harvested and used for power generation [10,11].

The past decades have seen an increasing variety of theoretical treatments, providing further insight into the phenomenon. One of the earliest works falling into this category was done by Kornecki et al. [12], where the instability has been analyzed using a potential flow with a linear solid model, see also [13] with improved computer accuracy. Eloy et al. [13] also developed a three-dimensional

\* Corresponding author at: Laboratoire de Mécanique, Modélisation et Procédés Propres (M2P2), CNRS et Aix-Marseille Université, France. Tel.: +49 17683252194.

E-mail addresses: [thomas.engels@l3m.univ-mrs.fr](mailto:thomas.engels@l3m.univ-mrs.fr), [thomas.engels@mailbox.tu-berlin.de](mailto:thomas.engels@mailbox.tu-berlin.de) (T. Engels).

finite-span model and explained why the two-dimensional theoretical predictions are not observed experimentally. There is also a viscous stability analysis available, developed by Connell and Yue [3], which we will also use for comparison. The same study presents some explanation for the bistable character, yet this question is not completely understood. For an exhaustive review on theoretical stability analysis, we refer to [14,15].

Since the pioneering experiments performed by Taneda [16], dealing with a flag in a wind tunnel, several experimental studies have been published. Shelley et al. [17] studied the problem in a water tunnel and found the flapping frequency to increase linearly with the inflow velocity, a fact that is observed also in the present work. Eloy et al. [13] performed wind-tunnel experiments and confirmed their state-of-the-art analysis, taking a finite span into account.

Since fluid–structure interaction is computationally challenging, both in terms of computational power and numerical modeling, the numerical simulations concentrate mostly on the last decade. They can be subdivided in two major categories, depending on the fluid model: inviscid and viscous approaches.

Among the inviscid methods, i.e. methods that are using some kind of approximation for the fluid instead of evaluating the complete Navier–Stokes equations, two examples are the vortex sheet method presented by Alben [6] and the discrete vortex shedding method developed by Michelin et al. [18]. The latter is used for comparison with present results.

One of the first simulations solving the complete Navier–Stokes equation was developed by Zhu and Peskin [19]. They used a new version of the immersed boundary method to take the structure into account, incorporating its mass as a delta function layer of the fluid density. Their simulations, performed at  $Re = 200$ , showed that a minimum mass of the filament is required to sustain flapping and that bistability depends on the filament's length. The latter observations are in agreement with the experiments of Zhang et al. [20]. Sawada and Hisada [21] also reproduced the experiments of Zhang et al. [20] using an arbitrary Lagrangian–Eulerian approach. The immersed boundary method for the filament has been improved by Huang et al. [22]. The latter study also considered two foils, coupled by the ambient fluid.

A different approach was employed by Connell and Yue [3], based on body-fitted grids. They confirmed that a massless filament is always stable and found good agreement with the viscous linear stability analysis presented in the same work. This study is the most detailed one considering the complete Navier–Stokes equations, but rather coarse grids have been used.

Balint and Lucey [23] focused on the application to snoring and airway collapse, their numerical simulations are performed at a Reynolds number in the same range as in the present paper. The beam was modeled using a simple linear model for the solid. Another type of solid model is also employed in the work of Farnell et al. [24], where the beam is represented by an ensemble of tiny rigid objects, connected by springs. This approach apparently requires more development, especially in tuning the parameters.

The main novelty of the present work is the extension of a viscous incompressible fluid solver previously developed in [1] to take flexible solids into account. A fluid–structure coupling technique is proposed that is compatible with the volume penalization method and Fourier pseudo-spectral discretization. The coupled fluid–structure interaction solver is applied to study the flutter problem. We present high-resolution simulations that resolve the far field of the flow as good as the vicinity of the structure. Moreover, the spectral discretization does not introduce numerical dissipation. The simulations show that a chaotic state does not necessarily have to occur directly after the initial perturbation, but that it rather can take a finite time, during which the flapping

is periodic, before developing such a state. This result is obtained using a time–frequency decomposition based on wavelets.

The remainder of this article is organized as follows. In Section 2 we describe the computational setup and the governing equations for both the fluid and the solid part, as well as the volume penalization method. Numerical algorithms used to solve the coupled problem are presented in Section 3. In Section 4, we then apply our new method to the fluttering instability. Numerous simulations are performed to explore the influence of the Reynolds number and the reduced inflow velocity on the non-linear dynamics of the coupled fluid–structure system. Finally, some conclusions are drawn in Section 5.

## 2. Setup and governing equations

### 2.1. Computational setup

The computational setup for our simulations is illustrated in Fig. 1. The slender structure,  $\Omega_s$ , is clamped at its leading edge and placed on the axis of symmetry. Its thickness is assumed to be small, such that the finite thickness  $t$  entering the simulation is a numerical parameter rather than a physical one, as explained in Section 3.1.4. The distance  $x_0$  is one chord length  $\ell$ .

The mean flow in the fluid  $\Omega_f$  is parallel to the initially undeformed, straight structure. At all four boundaries of the domain we impose homogeneous Dirichlet conditions on the vorticity using a sponge technique acting on the domain  $\Omega_{sp}$ , as specified in Section 3.1.2.

The flow is given a sufficiently long time to develop a boundary layer in the vicinity of the fluid–solid interface. Then, an external force is applied on the structure, bending it downwards to break the symmetry. Depending on the system parameters, the beam may return to its rest position (stable) or sustain either a periodic or chaotic flutter motion.

For convenience, we render all equations and quantities dimensionless, with the free-stream velocity  $u_\infty$ , the fluid density  $\varrho_f$  and the beam length  $\ell$  being the set of reference values. Three dimensionless parameters determine the response to the initial perturbation: the Reynolds number  $Re$  and two parameters characterizing the elastic material, its normalized bending resistance  $\eta$ , and density  $\mu$ , given by

$$Re = \frac{u_\infty \ell}{v}, \quad \mu = \frac{\eta \varrho_s}{\ell \varrho_f}, \quad \eta = \frac{Eh^3}{12\ell^3 \varrho_f u_\infty^2}, \quad (1)$$

respectively. Here,  $\varrho_s$  is the solid density,  $E$  its Young's modulus and  $h$  the (physical) height of the cross section, which is not the same as the numerical thickness  $t$  that is used to define the geometry of the problem, cf. Fig. 1. Due to the normalization, both  $\mu$  and  $\eta$  characterize the solid material as much as the fluid flow.

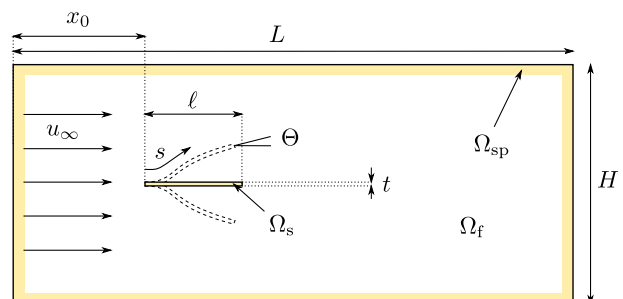


**Fig. 1.** Fluid–structure configuration with constant uniform mean flow and a clamped flexible beam. The rectangular computational domain  $\Omega$  comprises the fluid domain  $\Omega_f$ , the solid domain  $\Omega_s$  and the sponge layer  $\Omega_{sp}$ .

## 2.2. Fluid model

We consider an incompressible Newtonian fluid with constant density, in the fluid domain  $\Omega_f$ , governed by the Navier–Stokes equations. No-slip boundary conditions at the fluid–solid interface  $\partial\Omega$  and an initial condition complete the problem

$$\begin{aligned} \partial_t \underline{u} + (\underline{u} \cdot \nabla) \underline{u} &= -\nabla p + \frac{1}{\text{Re}} \Delta \underline{u}, \quad \nabla \cdot \underline{u} = 0, \\ \underline{u}|_{\partial\Omega} &= \underline{u}_s(s, t), \quad \underline{u}(x, t = 0) = \underline{u}_0(x). \end{aligned} \quad (2)$$

The interface is allowed to move and to deform, interacting in non-linear fashion with the surrounding fluid and thereby constituting the numerical challenge of the problem at hand. Numerous computational techniques are available for its solution, for example one could use a rather traditional approach using body-fitted, structured or unstructured grids [25,26]. This comprises a complicated re-meshing process and data transfers between different grids. There are some alternative approaches that allow to avoid re-meshing, such as the Lattice-Boltzmann solvers, Smooth Particle Hydrodynamics or vortex methods. Another popular approach is the use of ALE (arbitrary Lagrangian–Eulerian) methods, that also avoid remeshing, see for example [27]. It is also possible to keep the Eulerian description of the fluid and use immersed boundary methods to account for the moving boundaries. This approach is chosen in the present work.

We use the volume penalization method to treat the no-slip boundary conditions. In general, penalization methods consist in embedding the original, complex spatial domain into a bigger domain with simple geometry, cf. [28,29]. The boundary conditions are then enforced by supplementary terms in the original equations. In particular, the volume penalization method uses the Darcy force to model the solid objects. This is inspired by the idea of considering impermeable walls as permeable ones with small, and, in the limit, vanishing permeability. The main advantage of this procedure is the fact that now all information about the geometry is included in the penalization term, hence there is no need to account for it when discretizing the equations. This method has first been proposed by Arquis and Caltagirone [30] for flows in porous media. Angot et al. [31] presented a mathematically rigorous proof for the convergence of the penalized incompressible Navier–Stokes equations to the original equations with no-slip boundary conditions. The rate-of-convergence estimates were refined by Carbou and Fabrie [32]. The penalization method has been used successfully to compute the flow around fixed obstacles of complex shape, see for example [33–35], and extended to simulate moving, rigid objects by Kolomenskiy and Schneider [1].

The penalized version of (2) reads

$$\partial_t \underline{u} + (\underline{u} \cdot \nabla) \underline{u} = -\nabla p + \frac{1}{\text{Re}} \Delta \underline{u} - \frac{\chi}{\varepsilon} (\underline{u} - \underline{u}_s), \quad \nabla \cdot \underline{u} = 0, \quad (3)$$

The Darcy penalization term,  $\chi/\varepsilon(\underline{u} - \underline{u}_s)$ , contains all the geometry of the problem. The mask function  $\chi$  is  $\chi = 0$  if  $\underline{x} \in \Omega_f$  and  $\chi = 1$  if  $\underline{x} \in \Omega_s$ , where  $\underline{u}_s(\underline{x}, t)$  is the velocity of the solid and  $\underline{x} \in \Omega$  the position vector. The parameter  $\varepsilon$  is the penalization parameter, physically interpreted as the permeability of the solid. The solution of the penalized problem converges to the solution of the original problem with an order of convergence of  $\mathcal{O}(\sqrt{\varepsilon})$  [32]. In this connection it has to be emphasized that  $\varepsilon$  is a numerical parameter that can, unlike the spatial resolution, be chosen a priori as small as necessary. For a detailed mathematical analysis of the penalized differential operators and their discretization we refer to [36].

Another advantage is that the hydrodynamic forces can be computed using volume integrals instead of evaluating surface integrals,

$$F = \int_{\Omega_s} \frac{\chi}{\varepsilon} (\underline{u} - \underline{u}_s) d\Omega + \frac{d}{dt} \int_{\Omega_s} \underline{u}_s d\Omega. \quad (4)$$

The second contribution is the unsteady correction for moving and deforming objects [37,1]. As we suppose the problem being two-dimensional, it is appealing to work with the vorticity–velocity formulation of the Navier–Stokes equations. This yields a scalar-valued equation where the incompressibility of the velocity field is satisfied via the Biot–Savart relation. The penalized Navier–Stokes equation, written in vorticity–velocity formulation, reads

$$\partial_t \omega + (\underline{u} \cdot \nabla) \omega = \frac{1}{\text{Re}} \Delta \omega - \nabla \times \left( \frac{\chi}{\varepsilon} (\underline{u} - \underline{u}_s) \right). \quad (5)$$

The velocity is determined as  $\underline{u} = \nabla^\perp \psi + \underline{u}_\infty$ , where the stream-function  $\psi$  is the solution of  $\nabla^2 \psi = \omega$  and  $\nabla^\perp = (-\partial_y, \partial_x)^T$  is the orthogonal gradient. The free-stream velocity is denoted by  $\underline{u}_\infty$ . Note that  $\underline{u}_\infty$  has to be irrotational, but it may well depend on time. To compute the pressure field from the vorticity and the velocity, we take the divergence of the Navier–Stokes equation in primitive variables, yielding a Poisson equation for the pressure,  $-\nabla^2 q = \nabla \cdot (\underline{\omega} \times \underline{u}) + \nabla \cdot \chi/\varepsilon(\underline{u} - \underline{u}_s)$ , where  $q = p + 0.5 \underline{u}^2$  is the dynamical pressure.

## 2.3. Solid model

The solid part is considered as a slender, inextensible beam, consisting of a linear-elastic material satisfying Hooke's law. Such a structure is essentially one-dimensional. We use a model that allows large deflections, it hence includes geometrical non-linearity. The structural contribution to the total dissipation is small compared to the fluid's one and therefore neglected.

The dynamics of the structure is determined by the pressure difference between the upper and lower side of the beam, viscous stresses are neglected. A similar hypothesis was made in [3], where only the normal stresses were taken into account, because the normal stresses are dominated by the pressure at the regimes which we consider here. In the vortex shedding simulations [18], viscous tensions are not modeled neither.

These assumptions lead to two coupled non-linear partial differential equations,

$$T_{ss} - T \Theta_s^2 = -[p]^\pm \Theta_s - 2\eta \Theta_s \Theta_{sss} - \eta \Theta_{ss}^2 - \mu(\dot{\Theta})^2 \quad (6)$$

$$\mu \ddot{\Theta} = -[p]_s^\pm - \eta \Theta_{ssss} + (T + \eta \Theta_s^2) \Theta_{ss} + 2T_s \Theta_s, \quad (7)$$

where  $T$  is the tension inside the beam that guarantees its inextensibility,  $[p]^\pm$  is the local pressure difference between upper and lower side,  $\Theta$  the local deflection angle,  $s \in [0, 1]$  the reduced arc length coordinate,  $(\cdot)_s$  and  $(\cdot)$  denote the derivatives with respect to  $s$  and time, respectively. The parameters  $\mu$  and  $\eta$  are the reduced density and stiffness, respectively, as defined in Section 2.1.

The beam is clamped at the leading edge, so its local deflection angle is zero at this position, as well as the local acceleration. The trailing edge is a free end, therefore all tensions are zero. Thereby we find the complete set of six boundary conditions, yielding

$$\left. \begin{array}{l} \Theta = 0 \\ T_s + \eta \Theta_{ss} \Theta_s = 0 \\ T \Theta_s - \eta \Theta_{ss} = [p]^\pm + \mu f_{\text{ext}} \end{array} \right\} \quad \begin{array}{l} \text{at } s = 0, \quad \Theta_s = 0 \\ \Theta_{ss} = 0 \end{array} \quad \left. \begin{array}{l} T = 0 \\ \Theta_s = 0 \\ \Theta_{ss} = 0 \end{array} \right\} \quad \text{at } s = 1, \quad (8)$$

where  $f_{\text{ext}}$  is the external force used to trigger the instability, as described in Section 4.

## 3. Numerical method

### 3.1. Fluid solver

#### 3.1.1. Spatial discretization

The spatial discretization of the penalized Navier–Stokes equations (5) is performed using a Fourier-pseudospectral scheme. The

vorticity and all other variables are represented as truncated Fourier series,

$$\omega(\underline{x}, t) = \sum_{k_x=-N_x/2}^{N_x/2-1} \sum_{k_y=-N_y/2}^{N_y/2-1} \hat{\omega}(\underline{k}, t) \exp(i\underline{k} \cdot \underline{x}),$$

where  $\underline{k} = (k_x, k_y)^T$ . The Fast Fourier Transformation with its order  $N_x N_y \log_2(N_x N_y)$  complexity is used to switch between physical and Fourier space. Derivatives are computed in Fourier space by multiplication by  $i\underline{k}$  and  $-|\underline{k}|^2$  for the gradient and the Laplacian, respectively. The non-linear term  $(\underline{u} \cdot \nabla) \omega$  and the penalization term  $\nabla \times (\frac{\chi}{\varepsilon} (\underline{u} - \underline{u}_s))$  are evaluated by the pseudo-spectral technique using collocation in physical space. This avoids the expensive computation of convolution integrals in Fourier space. Solving a Poisson equation, as required for the streamfunction and the pressure, reduces to a division by  $|\underline{k}|^2$ . To avoid aliasing errors, i.e. the production of small scales due to the non-linear terms which are not resolved on the grid, we de-alias the vorticity at each time step by truncating its Fourier coefficients using the 2/3 rule [38]. The Fourier pseudospectral method offers the advantage of absent numerical diffusion and a straightforward implementation.

### 3.1.2. Boundary conditions

By using this type of discretization, the computational domain  $\Omega = \Omega_f \cup \Omega_s \cup \Omega_{sp}$  is assumed to be periodic in both  $x$  and  $y$  direction. This is, usually, in conflict with the physical situation and makes the Fourier pseudospectral method solely suitable for physically periodic configurations, such as homogeneous turbulence, or requires very large computational domains to reduce the influence of the ghost images.

The range of applications of this discretization can be improved with the help of the volume penalization method. All we need to do is to use suitable penalization terms to force the desired inflow condition.

We add a penalization term for the vorticity, i.e.  $\chi_{bc}/\varepsilon_{bc}(\omega - \omega_0)$ , to Eq. (5) in order to impose a Dirichlet condition on  $\omega$ , typically with  $\omega_0 = 0$ . The mask function for the sponge,  $\chi_{bc}$ , is defined like a frame around the computational domain, as illustrated in Fig. 1. There is no need for the use of two distinct penalization parameters, since both have the same convergence properties and imply the same restrictions on the time step. Hence we set  $\varepsilon_{bc} = \varepsilon$ . Using this technique is particularly suitable for free-flow configurations and therefore used for the simulations in Section 4. Fig. 2 illustrates the effect of the sponge. In the periodic case (left), the wake of the obstacle re-enters the domain. The penalization term for the vorticity cancels the wake and prevents it from an interaction with the obstacle.

### 3.1.3. Time discretization

Having performed the spatial discretization, we still need to discretize Eq. (5) with respect to time. It is possible to rewrite Eq. (5) in the form of a non-linear evolution equation,

$$\partial_t \omega - \frac{1}{Re} \Delta \omega = f(\omega), \quad (9)$$

where the convection and penalty terms are now assembled in the non-linear function  $f(\omega)$ . First we consider the homogeneous equation where  $f = 0$ . The Laplace operator is diagonal in Fourier space, therefore we can easily find the exact solution of the homogeneous equation,

$$\hat{\omega}(\underline{k}, t^{n+1}) = \hat{\omega}(\underline{k}, t^n) \exp\left(-\frac{\Delta t}{Re} |\underline{k}|^2\right),$$

where the time step  $\Delta t = t^{n+1} - t^n$  has been introduced. The solution of the complete Eq. (9) is then given by

$$\begin{aligned} \hat{\omega}(\underline{k}, t^{n+1}) &= \hat{\omega}(\underline{k}, t^n) \exp\left(-\frac{\Delta t}{Re} |\underline{k}|^2\right) + \int_{t^n}^{t^{n+1}} \\ &\quad \times \exp\left(-\frac{\tau}{Re} |\underline{k}|^2\right) \hat{f}(\omega(\underline{x}, t^{n+1} - \tau)) d\tau. \end{aligned}$$

The integral on the right hand side can be evaluated by any quadrature rule. In the present work, an explicit Adams–Bashforth scheme of second order is used. Due to its explicit nature, the time step for this scheme is limited to  $dt \leq \min(CFL \Delta x / u_{max}, \varepsilon)$  for stability reasons. Note that the penalization term introduces additional stiffness and can therefore further limit the time step, provided  $\varepsilon$  is smaller than the CFL constraint [1,33]. However, the diffusion term is treated exactly and does not impose any stability limit on the time step.

### 3.1.4. Time-dependent penalization

Formally, it is straightforward to apply the volume penalization method in the case of moving and deforming obstacles, in which  $\chi$  depends on time. However, discretization of the time-dependent penalization term needs some particular treatment, as previously demonstrated in [1] for moving, rigid objects. The problem arises from the fact that  $\chi$  is actually discontinuous and can therefore not be displaced smoothly. The minimum displacement is one grid point, yielding a CFL number of one. This jerky motion of a discontinuous mask causes large numerical oscillations in the hydrodynamic forces. A possible way to circumvent this problem is to shift the mask in Fourier space, as described in [1]. However, this approach is only suitable for rigid moving bodies.

The technique used in the present work relies on using a smooth mask rather than a discontinuous one. Hence we choose a continuous approximation to the Heaviside function, with a certain width of the transition from one to zero. The width of this smoothing layer decreases when the resolution increases, so the smooth approximation gets sharper and converges, in the limit of small  $\Delta x$ , to the Heaviside function. This smooth function can then be displaced by an increment as small as desired and not limited by the spatial resolution. Among the various possible approximations we choose

$$\chi(x) = \frac{1}{2} \left[ \text{erf}\left(\frac{t-x}{\delta}\right) + \text{erf}\left(\frac{t+x}{\delta}\right) \right]$$

where

$$\delta = c_{sm} \Delta x \max\left(\frac{\partial \chi}{\partial x}\right) = \frac{c_{sm} \Delta x}{\sqrt{\pi}} [\exp(-4) - 1].$$

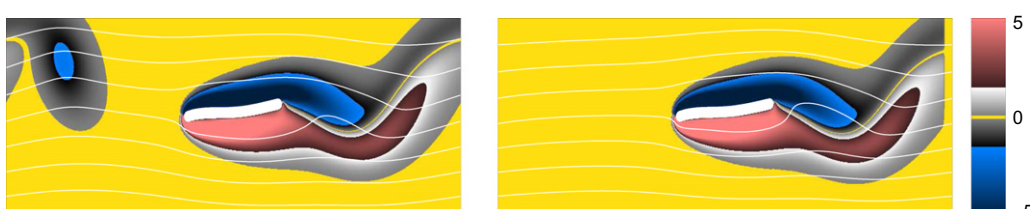


**Fig. 2.** Flow past an object without (left) and with (right) sponge technique. Shown is vorticity with superimposed white streamlines. Only part of the computational domain is shown.

The parameter  $c_{sm}$  defines the thickness of the smoothing layer in mesh widths.

### 3.2. Solid solver

The beam equation is solved numerically using a second order finite difference scheme for spatial discretization. All derivatives are approximated by central finite differences, at the boundaries we use fourth order backward stencils. As the beam equation is mathematically stiff, we apply a second order Crank–Nicolson scheme, and treat all terms implicitly. This avoids the use of very small time steps which would be required for an explicit time marching method. The evolution equation for  $\Theta$ , (7), contains a second order derivative in time, and is rewritten as a first order problem,

$$\begin{pmatrix} \Theta^{n+1} \\ \dot{\Theta}^{n+1} \end{pmatrix} = \begin{pmatrix} \Theta^n \\ \dot{\Theta}^n \end{pmatrix} + \frac{\Delta t}{2} \left( \begin{pmatrix} \dot{\Theta}^{n+1} \\ g(\Theta^{n+1}, T^{n+1}) \end{pmatrix} + \begin{pmatrix} \dot{\Theta}^n \\ g(\Theta^n, T^n) \end{pmatrix} \right), \quad (10)$$

where  $g(\Theta, T) = (-[p]_s^\pm - \eta\Theta_{ssss} + (T + \eta\Theta_s^2)\Theta_{ss} + 2T_s\Theta_s)/\mu$  denotes the right hand side of Eq. (7). The inextensibility equation for the tension  $T$ , (6), does not contain a time derivative of  $T$ . We denote this equation with  $h(\Theta, T)$  and add it to the system (8) at the new time level,

$$\begin{pmatrix} \Theta^{n+1} \\ \dot{\Theta}^{n+1} \\ 0 \end{pmatrix} = \begin{pmatrix} \Theta^n \\ \dot{\Theta}^n \\ 0 \end{pmatrix} + \begin{pmatrix} \frac{\Delta t}{2} (\dot{\Theta}^{n+1} + \dot{\Theta}^n) \\ \frac{\Delta t}{2} (g(\Theta^{n+1}, T^{n+1}) + g(\Theta^n, T^n)) \\ h(\Theta^{n+1}, T^{n+1}) \end{pmatrix}. \quad (11)$$

The system (11) is a non-linear set of equations with the unknown deflection angle  $\Theta$  and tension  $T$  at the new time level. To solve it numerically, we perform Newton–Raphson iterations and use the solution of the previous time step as initial guess for the unknowns. Performing Newton–Raphson iterations requires the knowledge of the Jacobian, which we compute analytically. The resulting linear systems are solved using a fast sparse matrices solver, PARDISO, see [39]. In each time step, 2–3 iterations are performed, and the computational cost of the solid solver is less than 1% of the total cost.

### 3.3. Numerical coupling

The numerical challenge when simulating fluid–structure interaction constitutes in the coupling of the two physical fields. Physically, the coupling conditions consist in the no-slip conditions of the velocity and the continuity of the mechanical stress tensor at the fluid–solid interface. The former condition, a kinematic one, is treated by the volume penalization method, we only need to provide the obstacle's position ( $\chi$ ) and its velocity ( $\underline{u}_s$ ).

The pressure field is continuous in the computational domain  $\Omega$ , but we need to provide the surface pressure to the solid solver. As the beam nodes do usually not coincide with the grid points, we use a bi-cubic interpolation of the pressure. We found that a simple linear interpolation is not sufficient and can lead to considerable spurious oscillations in the forces, resulting in numerically induced oscillations, possibly amplified by resonance phenomena.

In order to discuss the numerical coupling scheme, we first introduce some notation. Let  $\mathcal{S}$  and  $\mathcal{F}$  be the solid and fluid operators, respectively, and  $b$  and  $f$  the beam and the fluid state. Then we can note the problem at hand

$$\dot{f} = \mathcal{F}(b, f), \quad \dot{b} = \mathcal{S}(b, f). \quad (12)$$

Introducing the time and space discrete operators  $\mathbb{S}$  and  $\mathbb{F}$ , we can describe the coupling scheme used in this work by

$$f^{n+1} = \mathbb{F}(f^n, b^n), \quad b^{n+1} = \mathbb{S}(b^n, f^{n+1}).$$

Thus we first advance the fluid, keeping the solid fixed during the time step. Then we obtain the new forces on the beam using the fluid field at the new time step,  $f^{n+1}$ . These are then transferred to the solid solver to advance the beam to the next time level and construct the mask function for the next time step.

Using this scheme, the coupling is realized explicitly, and the scheme is called “sequential staggered”. It is first order accurate in time. Coupling information is exchanged only once per time step, which is typical for a staggered scheme. Obviously, the dynamic coupling condition is fulfilled at the new time level  $n+1$ , but the kinematic condition is not. Explicit schemes can only fulfill either of them, but require only one call of each solver per time step.

Besides its appealing simplicity, this scheme has the drawback of a limited stability. It suffers from the artificial added mass effect, a numerical instability arising in incompressible simulations. Foerster et al. [40] carried out a detailed mathematical analysis of this effect, explaining why smaller time steps cannot stabilize the simulations. The stability depends on the mass ratio: very light immersed structures cannot be simulated using a staggered scheme. In such cases, a strong coupling algorithm has to be applied. For this purpose we implemented an iterative coupling algorithm. It is based on fixpoint iterations with an Aitken relaxation. Several tests showed that both algorithms yield nearly identical results for heavy structures, and that hence the violation of the kinematic coupling condition does not alter the results. The only visible difference is the stability for light structures, where the staggered scheme fails.

In the present paper, we do not consider very light structures and therefore work only with the faster staggered scheme.

### 3.4. Validation results

The present numerical scheme has been successfully compared with the benchmark proposed by Turek and Hron [41]. It consists of three stages, a CFD (computational fluid dynamics) test with a fixed obstacle, the CSM (computational structural mechanics) test where only the solid is considered, and the fully coupled FSI (fluid–structure interaction) test.

The CFD test consists in a channel flow with an immersed, rigid object, for different Reynolds numbers (20, 100 and 200). The quantities of comparison are the hydrodynamical lift and drag forces. The converged values of the present solver differ about 0.90% from the reference values.

The CSM test deals with the structure only, under the load of gravity, and is used to validate both the solid model and the corresponding numerical solver, yielding a difference of about 1% in both displacement amplitude and frequency.

Finally, the coupled FSI test completes the validation. Herein, a flexible foil is placed in a channel and in the wake of a fixed cylinder. The agreement is as good as for the other tests.

### 3.5. Influence of thickness and penalization parameter

The volume penalization method requires an obstacle occupying a certain volume to work. If the structure is too thin, possibly even thinner than the spatial resolution, we can no longer simulate it.

In the setup used for validation tests, a structure of finite thickness was considered. Therefore  $t$  is a given constant and we set the geometrical thickness equal to the physical thickness of the structure. The physical thickness is used to define the material properties, such as weight per unit length and bending resistance.

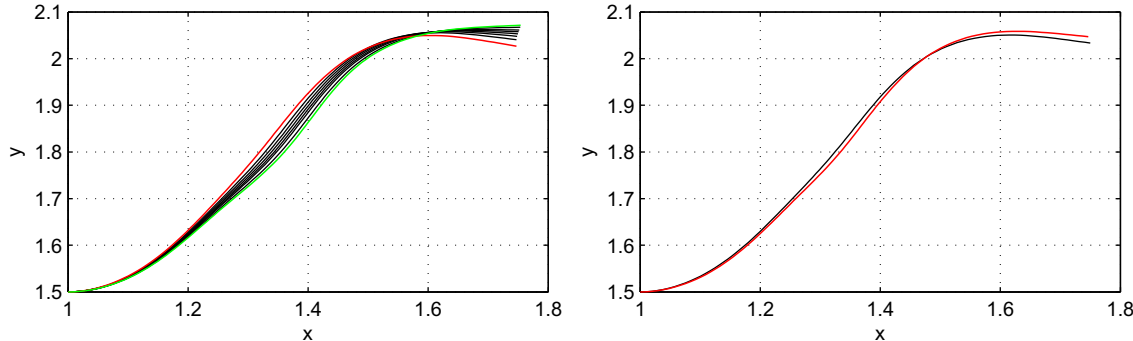


**Fig. 3.** Influence of the thickness (right) and the penalization parameter (left). Both figures show the deflection line of the beam. The mean flow has an orientation of 45°. Although the thickness varies by a factor of 10, the difference in deformation between the thinnest (red) and thickest (green) beam is less than 8%. The penalization parameter is decreased from  $\varepsilon = 10^{-3}$  (black) to  $\varepsilon = 5 \times 10^{-5}$  (red) and the difference is even smaller. We can conclude that both  $t$  and  $\varepsilon$  do not have a strong influence on the results. (For interpretation of the references to color in this figure legend, the reader is referred to the web version of this article.)

In the present work, we focus on the flutter phenomenon and deal with a slender structure. Therefore the thickness  $t$  is a numerical parameter rather than a fixed value given by the geometry. It is now natural to ask how sensitive the solution depends on this parameter. To clarify this, we performed some simulations in a smaller domain ( $3 \times 3$ ) with high resolution ( $1200 \times 1200$ ), in order to allow for a large range of thicknesses. The mean flow is oriented with an angle of 45° with respect to the initial beam. It is likely that the thickness has a stronger influence on the dynamics than in the case where the mean flow is parallel to the beam, because it acts more like a bluff body.

We compute this simulation for different thicknesses,  $t = 6.25 \times 10^{-3}, 1.25 \times 10^{-2}, 1.88 \times 10^{-2}, 2.50 \times 10^{-2}, 3.13 \times 10^{-2}, 3.75 \times 10^{-2}, 5.0 \times 10^{-2}, 6.25 \times 10^{-2}$ . The smallest value corresponds to 5 grid points, while the largest one corresponds to 50 grid points. Fig. 3 (left) illustrates the deflection lines (i.e. the actual coordinates of the beam nodes) for this range of thicknesses. Although we vary  $t$  by a factor of 10, the resulting deflection lines alter only by about

$$\frac{y(s=1)_t - y(s=1)_{t_{\min}}}{y(s=1)_{t_{\min}} - y_0} = 8\%.$$

Note that  $t = 6.25 \times 10^{-2}$  can barely be called slender. To clarify the influence of  $\varepsilon$ , we fix the thickness and vary  $\varepsilon$  between  $10^{-3}$  and  $5 \times 10^{-5}$ . Fig. 3 (right) exhibits that the influence of  $\varepsilon$  is even smaller, the deflection lines of the smallest and the largest  $\varepsilon$  differ only by about 2%. We can hence conclude that the solution is not very sensitive to either of these parameters, as long as they are chosen reasonably. Of course, a very thick beam or a very large  $\varepsilon$  would not yield physical results.

#### 4. Results

We now apply the method described above to study the flutter problem. The domain size is  $L \times H = 10 \times 4$  chord lengths, the vorticity sponge technique is applied at all four boundaries of the domain and thus prevents the wake from re-entering the domain. The spatial resolution is  $2000 \times 800$  Fourier modes for  $Re \leq 200$ ,  $2500 \times 1000$  for  $Re = 500$ ,  $2800 \times 1120$  for  $Re = 750$  and finally  $3200 \times 1280$  for  $Re = 1000$ . The penalization parameter is fixed to  $\varepsilon = 10^{-4}$  and the smoothing is equal to two grid points, i.e.  $c_{sm} = 2$ , in all simulations. The beam thickness is  $4 \times 10^{-2}$ , corresponding to eight grid points on the coarsest and 13 on the finest grid. To complete the picture and to check its validity, some runs with double resolution have also been performed, yielding a difference of less than 3% for the averaged end point deflection angle

amplitude and about 8% for the lift force amplitude, with respect to the coarser simulations.

For the flutter phenomenon it is conventional to introduce a reduced free-stream velocity  $u^* = \sqrt{\mu/\eta} = u_\infty \ell \sqrt{Q_s/EI}$ , as proposed in [13,2,10,17]. There is no mathematical reason for this choice, but it is physically more intuitive to increase the flow velocity than decreasing the bending stiffness and hence change the material the beam is made of.

The setup is symmetric with respect to the beam, therefore the instability has to be triggered somehow. This is done by applying an external force,  $f_{ext}$  in Eq. (8), on the structure during a small time interval. At the end of this perturbation, the beam has moved downwards by about  $2 \times 10^{-3}$  units and reaches a velocity of  $2 \times 10^{-2}$ . Note that applying an external force is possibly the easiest way to break the symmetry, as this is always compatible with the boundary conditions (8).

In this study we keep the mass ratio fixed at  $\mu = 1/3$  and vary the Reynolds number and the reduced free-stream velocity. Fig. 4 summarizes the parameters for which the different simulations have been performed, where the symbols indicate configurations found to be stable (□) or in a periodic (○) or chaotic (★) fluttering state.

We compare our results with two different computational approaches. The first one is the inviscid vortex shedding model presented by Michelin et al. [18]. This study uses the same model equation for the beam as we do and a simplified model for the fluid. Their results concerning the stability limit are in agreement with the existing experimental and linear stability results presented in [13]. For the mass ratio considered here, stability is lost above  $u_{crit}^* = 9.6$ , according to their stability analysis. This stability limit is represented by the dash-dotted line in Fig. 4.

The second study we compare our results with the work of Connell and Yue [3], where a linear stability analysis for viscous flows and direct numerical simulations have been presented. The solid is also modeled using a non-linear beam equation. The computational approach for these simulations relies on body-fitted, time-dependent grids with a resolution of  $100 \times 200$  points. Spatial discretization is performed using second order finite differences. The linear stability analysis assumes a Blasius boundary layer on the beam to determine its internal tension, therefore the stabilizing force depends on the Reynolds number. Recasting the stability limit found by this analysis in our terminology, the beam becomes unstable at

$$u_{crit}^* = 2\pi \sqrt{\frac{\mu}{\frac{\mu}{\mu\pi+1} - 1.3 Re^{-1/2}}} \quad (13)$$

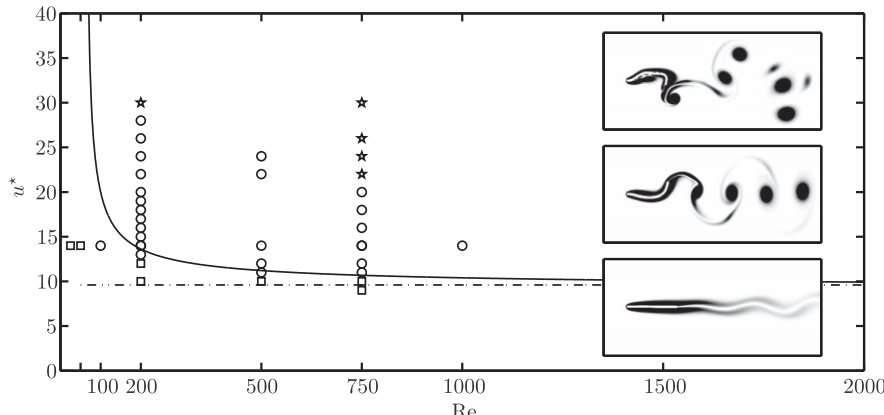


**Fig. 4.** Stability map in the  $Re - u^*$  plane for  $\mu = 1/3$ . Inviscid [18] (—) and viscous linear stability analysis [3] (—) Symbols indicate present simulations, found to be stable ( $\square$ ) or in an either periodic ( $\circ$ ) or chaotic ( $\star$ ) fluttering state. Insets show corresponding snapshots of the absolute vorticity  $|\omega|$  at  $Re = 750$ .

represented by the solid line in Fig. 4. The numerical simulations performed in [3] focus mainly on the limit of vanishing bending stiffness, with the mass ratio being the parameter of interest, and are found to be in reasonable agreement with the analytical results.

#### 4.1. Variation of the Reynolds number

In the first series of simulations, we focus on the influence of the Reynolds number for fixed values of  $\mu$  and  $u^*$ . In order to directly compare our results with the ones reported in [18], we fix  $\mu = 1/3$  and further choose  $u^* = 14$ . In the inviscid limit, this point was found to be in the chaotic regime. The considered Reynolds numbers are 25, 50, 100, 200, 500, 750 and 1000.

Fig. 5 illustrates the computations for  $Re = 25, 100, 200$  and 1000. The trajectory of the end point in the displacement–velocity plane illustrates the temporal behavior, and the vorticity field  $\omega$  at a given time is visualized in the vicinity of the beam. Note that the figure is a zoom and the computational domain is about two times larger in both directions. The  $Re = 750$  case is analyzed in detail in Fig. 6.

Let us first discuss the lowest Reynolds numbers, illustrated exemplarily for  $Re = 25$  in the top row of Fig. 5. In the phase diagram, the initial perturbation is marked by the red part of the trajectory. The oscillation amplitude grows during the first half turn in phase space, and then continuously spirals down to the initial state of rest.

Configurations marked as stable in Fig. 4 were stopped if the beam's internal energy, consisting of the elastic and kinetic contribution, stayed below the initial perturbation energy for sufficiently long time. We used  $T_{stop} = 15$ , which is larger than ten flapping cycles in a periodic case. In the vorticity snapshot, whose corresponding position in phase space is marked with a red star, a thick, attached boundary layer can be observed. The corresponding figures for  $Re = 50$  do not differ significantly, only the damping of the initial perturbation has become weaker and hence the typical spiral-like motion of the end point in phase space slower approaches its origin.

Increasing  $Re$  to 100, the behavior of the beam changes from stable to unstable. The phase diagram shows the growth in amplitude of the flutter oscillations, but also that this growth rate is very slow. Thus, we can conclude that the critical Reynolds number must be between 50 and 100, and that the distance to the upper limit of this range is smaller than the lower one. On the other hand, according to the viscous linear stability analysis, Eq. (13), the stability limit is predicted at  $Re_{crit} \approx 183$ . Hence we can confirm that the linear analysis tends to overpredict the stability threshold for

low Reynolds numbers, a result that has been stated in [3] for a different parameter range.

When further increasing  $Re$  to 200, the growth rate of the oscillation becomes significantly higher, as can be seen in the phase diagram in Fig. 5 (third row from top). The vorticity field shows distinct, separated vortices, shed each time the beam tip reaches its maximum amplitude. Note that the flow field for  $Re = 100$  is illustrated during the amplification phase. Comparing  $Re = 100$  and 200, the flow field reveals different wake structures in the amplification phase and in the final periodic state: during the growth phase, no distinct vortices are shed at the trailing edge of the foil, the wake is formed of two coherent zones of positive and negative vorticity. Furthermore, the final periodic state differs in both cases, while this is not true when comparing higher Reynolds numbers among themselves. The case  $Re = 100$  is therefore different from the others.

For  $Re = 500$ , the periodic state is reached sooner and the shed vortices become stronger and narrower, forming the characteristic von Kármán street, a trend that is preserved at  $Re = 750$  and 1000. Fig. 6 illustrates the vortex shedding mechanism observed at  $Re = 750$ . In snapshots A–B, the layer of negative vorticity on the top of the beam is sheared off the surface and elongated. The same holds for the layer of positive vorticity at the bottom side. Between C and D, a single vortex begins to separate, still connected to the remainder of the vorticity layer on the top side. The vortex is advected, and the reverse process starts (F–G). For the instant G, the whole vorticity field is shown, illustrating how the vortices eventually separate and form the street of isolated vortices. The process is also illustrated in the phase diagram in Fig. 6 (bottom left). The phase trajectories are colored by the absolute acceleration of the beam. Note that the acceleration varies smoothly. The shape of the beam, illustrated in Fig. 6 (bottom, right), is in good agreement with [18].

Even though there are some changes in the shape of the phase trajectory, the flapping amplitude remains constant above  $Re = 200$ . The same holds for the fundamental flapping frequency, that is the frequency of the trailing edge oscillations, as summarized in Table 1. The frequencies are computed using the fast Fourier transform, and the amplitude of the displacement,  $a_{disp}$ , is the averaged value of all periods after the amplification phase. This averaging is done as the beam does not reach a perfect periodic state during the computation. That can also be seen from the phase diagrams, where the trajectories are more spread out.

Hence we can conclude that we do not observe a transition to a chaotic state for this choice of parameters, contrary to the result from the inviscid model [18]. This may also be an effect due to

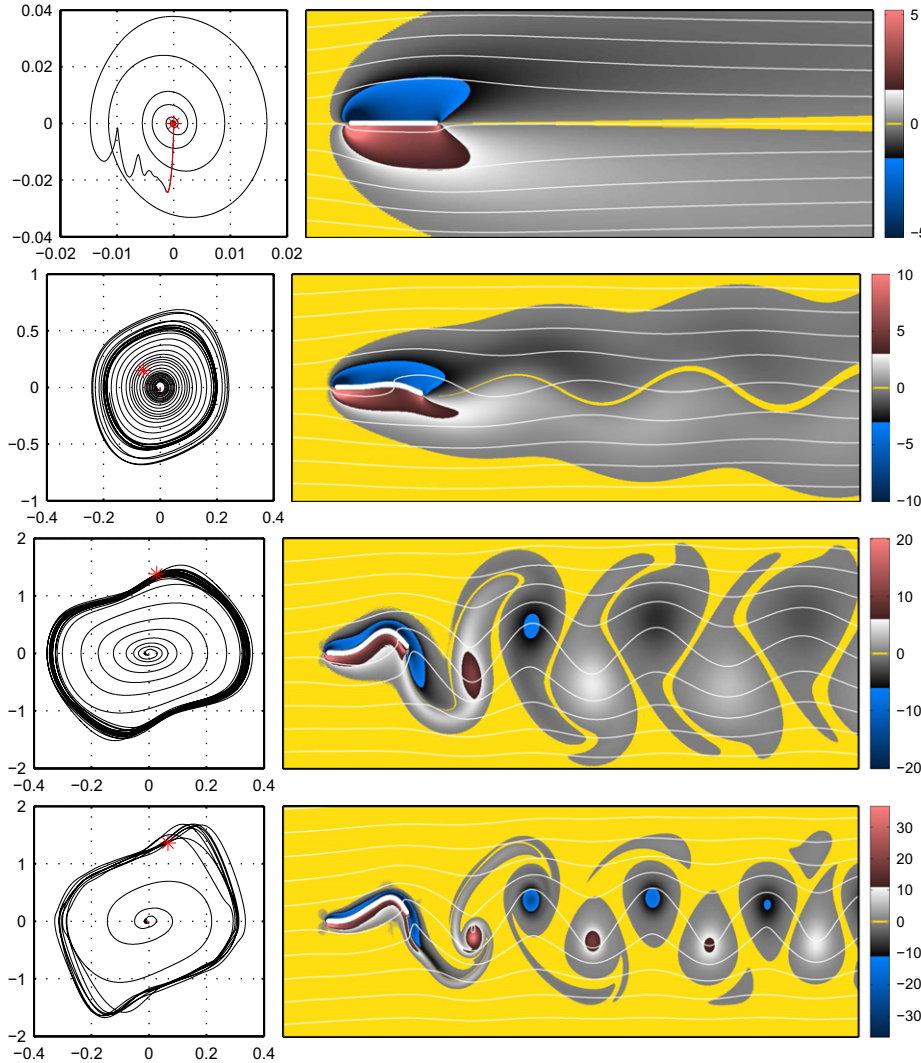


**Fig. 5.** The influence of the Reynolds number. Phase-diagram of the trailing edge in the displacement–velocity plane ( $y, u_y$ ) (left column) and a vorticity snapshot (right column) with superimposed white streamlines. Only part of the computational domain is shown. The Reynolds number is  $Re = 25, 100, 200, 1000$  (from top to bottom). The point in phase space belonging to the snapshot is marked with a red star. (For interpretation of the references to color in this figure legend, the reader is referred to the web version of this article.)

the finite simulation time, although the computation spans at least 20 oscillation periods.

#### 4.2. Influence of the stiffness and the transition to chaos

The first part of our parameter study dealt with the influence of the Reynolds number, now the influence of the stiffness is considered by varying the reduced inflow velocity. As illustrated in the stability diagram, Fig. 4, we focus on two different Reynolds numbers, 200 and 750, and increase the reduced inflow velocity from a stable state until we reach the region of chaotic flapping. A third series at  $Re = 500$  completes the picture.

Considering  $Re = 200$ , the onset of flapping can be observed for  $12 < u_{\text{crit}}^* < 13$ , while Eq. (13) predicts that to happen at 13.62. This slight difference between our results and the analytical model persists at  $Re = 500$ , where we find  $10 < u_{\text{crit}}^* < 11$  versus 11.21 from the theory. When  $Re$  is increased further, our interval matches the analytical prediction. As stated previously, a simulation is considered as stable if the internal energy of the beam remains smaller than its initial perturbation energy for sufficiently long time, despite some small oscillations that are not yet completely damped.

For the stability limit we can hence conclude that our results are in reasonable agreement with the viscous linear stability analysis, the difference becoming smaller with increasing Reynolds number. Note also that the prediction from the inviscid stability analysis [18] is consistent with the viscous theory for sufficiently high  $Re$ .

The present results for the transition from a regular to an irregular flapping state cannot be compared with the results reported in [3], since therein the limit of small bending stiffness is considered. In this limit, the transition periodicity–chaos is found to be well approximated by  $\mu_{\text{chaos}} = \beta \mu_{\text{crit}}$  with  $\beta = 2.5$ . In the case considered here, where the bending stiffness is not small, such a proportionality cannot be observed.

When the flapping state is periodic, a single vortex is shed at each up- and downstroke, as discussed in Section 4.1 and illustrated in Fig. 6. However, in the chaotic regime, the deformation at the trailing edge becomes larger (due to the increasing reduced inflow velocity), and now a pair of vortices of different sign is shed into the wake, see Fig. 8, labeled by X and Y. These dipoles propagate with an additional, self induced velocity, relative to the mean flow and thus form an irregular wake pattern. They can also travel in the cross-flow direction, as the dipole Y does. At most of the

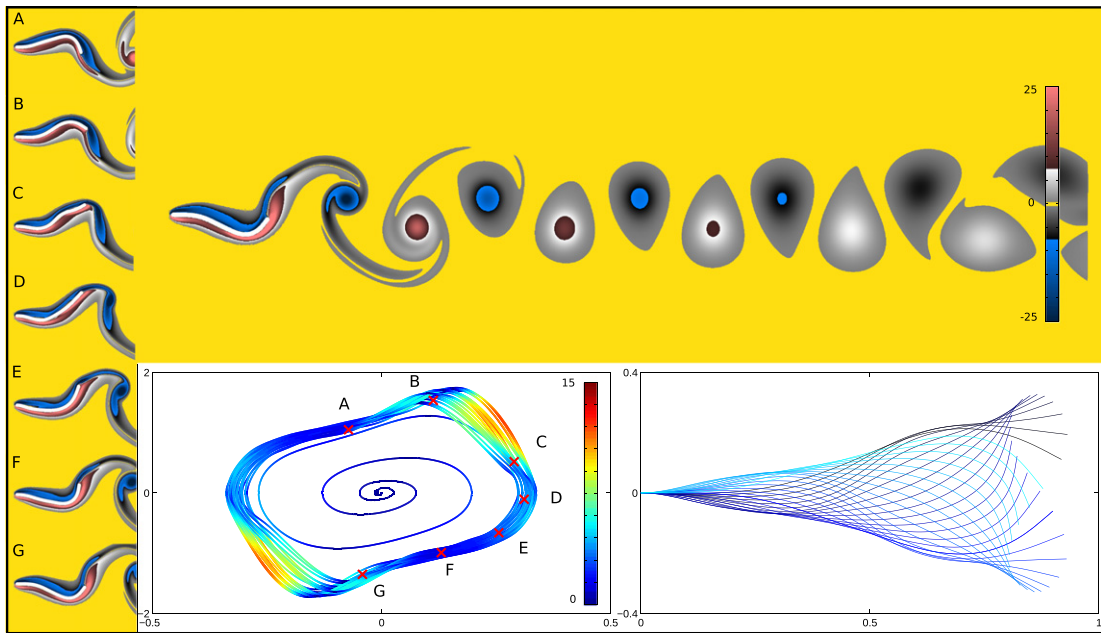


**Fig. 6.** Periodic state:  $Re = 750$  and  $u^* = 14$ . Left side: (A–G) time history of a typical oscillation period with a snapshot every  $\Delta t = 0.1$ . Top: the whole vorticity field at  $T = 84.5$ . Bottom, middle: Phase diagram of the end point, colored with the absolute acceleration. Bottom, right: time history of the deflection line for one period of motion, with  $\Delta t = 0.05$ , color ranging from dark to light blue. (For interpretation of the references to color in this figure legend, the reader is referred to the web version of this article.)

**Table 1**

Amplitude and frequency of  $y$ -displacement and frequencies of drag and lift forces as a function of the Reynolds number. The weight ratio is  $\mu = 1/3$  and the reduced inflow velocity is  $u^* = 14$ .

Re	$f_{\text{disp}}[u_\infty/\ell]$	$a_{\text{disp}}[\ell]$	$f_{\text{drag}}[u_\infty/\ell]$	$f_{\text{lift}}[u_\infty/\ell]$
100	0.4327	0.2020	0.8380	0.4138
200	0.5886	0.3368	1.1955	0.5886
500	0.6254	0.3186	1.2275	0.6254
750	0.6251	0.3142	1.2203	0.6251
1000	0.6161	0.3172	1.2321	0.6161

strokes, two vortices of approximately equal strength are shed (like the pair X).

However, the chaotic regime is also characterized by violent intermittent accelerations of the trailing edge, which are larger than the mean accelerations by an order of magnitude. In the phase diagram in Fig. 8, these violent snapping events are represented by strong peaks in the acceleration (indicated by the color). The mean absolute acceleration is found to be 5.7 and during snapping events peak values between 50 and 100 can be observed.

A single snapping event is illustrated in Fig. 8, left. The time instants A–G are equally spaced in time, with  $\Delta t = 0.05$ . The first three snapshots, A–C, show only minor evolution, illustrating the fact that the acceleration is small compared to the peak value between C and D, where the actual snapping takes place. Subsequently, a strong positive vortex is shed into the wake (E–G), followed by a less intense negative one (G).

This asymmetry in intensity of the shed dipole is also characteristic for the snapping event and distinguishes it from regular oscillations, where the dipole is approximately symmetric, compare dipole Z with X and Y in Fig. 8.

To further illustrate the chaotic nature of this regime, Fig. 8 contains also the time history of the beam deflection line. A distinct deflection line (Q) highlights another difference to the periodic state. The trailing edge of this deflection line is orientated against the flow direction, an event which does not occur in periodic simulations.

The differentiation between periodic and chaotic states, illustrated in Fig. 4, needs some further discussion. Several observations change during the transition. First, the relation between the frequencies of the displacement, and the lift and drag force differ in both flapping states. While we have  $f_{\text{disp}} = f_{\text{lift}}$  and  $f_{\text{drag}} = 2f_{\text{disp}}$  in a periodic state (cf. Table 1), these relations do no longer hold when the flapping is irregular. Moreover, we can no longer identify a dominant frequency in the spectra of the displacement and the hydrodynamic forces, as illustrated exemplarily by plotting the spectrum in Fig. 7 (right). This finding is consistent with the results reported in [3,18].

We observe from our data that chaos does not necessarily need to occur directly after the breaking of symmetry. Effectively, the initial perturbation may be followed by a phase of regular flapping, before this regularity breaks down and the beam performs chaotic oscillations. Therefore it is difficult to judge whether a configuration is chaotic or periodic. The last simulations marked as periodic in Fig. 4 did not show a transition for a long time ( $T_{\text{stop}} \geq 80$  corresponding to  $\approx 50$  periods), yet still it cannot be completely excluded that the periodicity will not break down. Note that in both [18,3] such a transitional behavior is not reported. However, [3] considers the limit of vanishing bending stiffness, and may therefore not be compared directly with the present results, and the method used in [18] relies on an inviscid approach. It can be conjectured that the finite Reynolds number inhibits the chaotic state for a certain time, and that this delay decreases with increasing  $Re$ .

To further investigate this transition, we apply the continuous wavelet transform (CWT) to the time evolution of the drag force. The CWT transforms the signal into the time-frequency domain [42]. We use the complex-valued Morlet wavelet with the wave-number  $k_\psi$  denoting the barycenter of the wavelet support in Fourier space. Here we use  $k_\psi = 5$ .

Fig. 9 shows the modulus of the wavelet-coefficients as a function of time and scaling factor (which is related to frequency), and the time history of the underlying drag signal on top, for  $Re = 750$  and  $u^* = 20$  and 22. The former case is the last value of  $u^*$  found to be in a periodic state and the latter is the first chaotic one. The

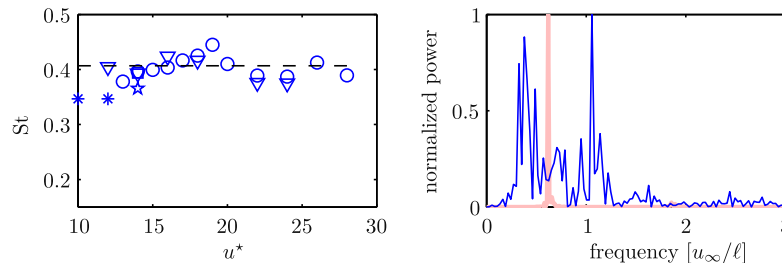


**Fig. 7.** Left: Strouhal number  $St = \frac{2 \cdot A_f}{u_\infty}$  of the displacement, for simulations resulting in periodic behavior.  $Re = 200$  ( $\circ$ ),  $Re = 500$  ( $\square$ ),  $Re = 750$  ( $\nabla$ ),  $Re = 1000$  ( $\star$ ) and values presented by Michelin et al. ( $*$ ) [18]. The dashed line corresponds to the average Strouhal number. Right: spectra of the integral lift force for  $Re = 750$  in a periodic ( $u^* = 14$ , light red) and chaotic ( $u^* = 30$ , blue) state. (For interpretation of the references to color in this figure legend, the reader is referred to the web version of this article.)

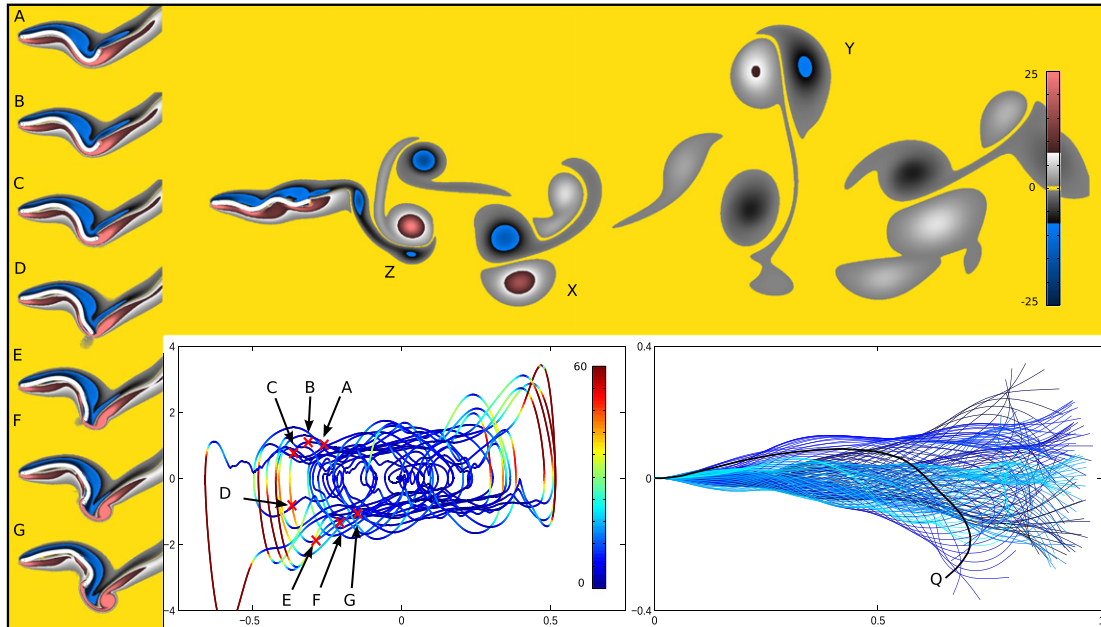


**Fig. 8.** Chaotic state:  $Re = 750$  and  $u^* = 30$ . Left side: (A–G) time history of a snapping event with a snapshot every  $\Delta t = 0.05$ . Top: the whole vorticity field at  $T = 11.70$ , exhibiting the typical vortex pairs of different sign ( $X$  and  $Y$ ), and the strongly asymmetric vortex pair resulting from the snapping event ( $Z$ ). Bottom, middle: Phase diagram of the end point, colored with absolute acceleration. Bottom, right: time history of the deflection line with  $\Delta t = 0.05$ , color ranging from dark to light blue. (For interpretation of the references to color in this figure legend, the reader is referred to the web version of this article.)

modulus of the wavelet-coefficients yields an energy distribution in the scale-time domain.

For the  $u^* = 20$  case, one distinct dominant frequency can be found, corresponding to a horizontal band in wavelet-space. This frequency does not alter significantly, albeit some deviations from

a purely periodic state can be observed. Note that the values for the lowest frequencies close to the beginning and the end of the signal are due to boundary effects.

Considering the  $u^* = 22$  case, a different behavior can be observed. The drag force exhibits a periodic behavior until  $T \approx 22$ ,

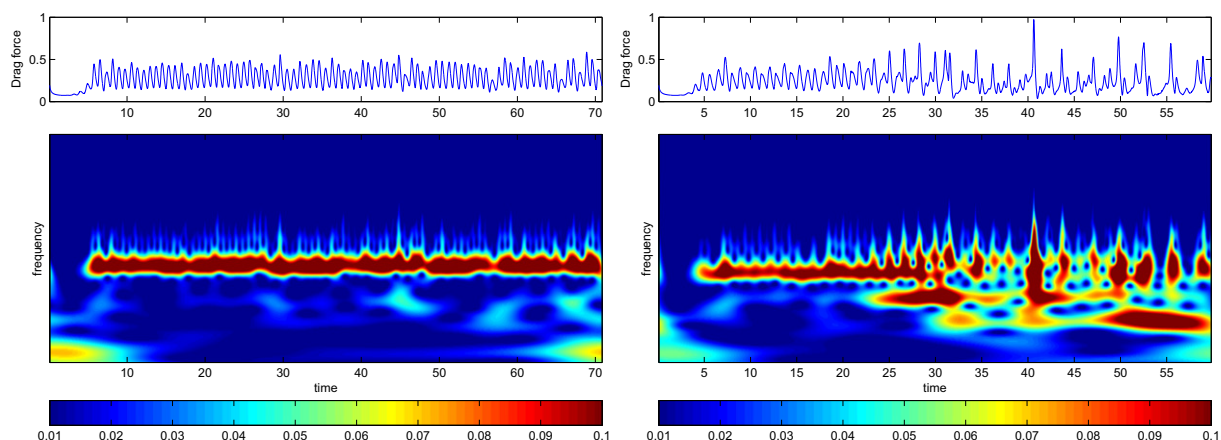


**Fig. 9.** Wavelet analyses of the drag force for case  $u^* = 20$  (left) and  $u^* = 22$  (right). The modulus of the complex valued Morlet wavelet coefficients are plotted as a function of position and scale. The original signal is plotted on the top.

similar to the  $u^* = 20$  case. After this time, a broad band of frequencies can be observed, characteristic for a chaotic state.

In periodic states, neither the flapping amplitude nor the frequency undergo a significant change when  $u^*$  is increased, hence the Strouhal number  $St = 2Af/u_\infty$  remains practically constant, as illustrated in Fig. 7. The standard deviation from the mean value, represented by the dash-dotted line, is 4.5% and there is no distinct trend visible. The comparison with the values reported in [18] yields reasonable agreement. In particular, the constant flapping frequency matches well the experimental results reported by Shelly et al. [17], where a linear dependency on the inflow velocity has been found. Therefore the frequency is a constant when normalized with  $u_\infty$ . The Strouhal number is constant, and does in particular not approach a “natural frequency of the fluid dynamics defined by a universal Strouhal number” [3] of  $St \approx 0.2$ . This result seems to somewhat contradict those of Connell and Yue [3]. They explained the transition to chaos with a resonance phenomenon when the flapping frequency matches this universal Strouhal number. A possible explanation may be that [3] considered the limit of vanishing bending stiffness, while here we deal with a finite one. We conjecture that the transition mechanism is different when the bending stiffness becomes larger.

## 5. Conclusions

A new computational approach using a Fourier pseudo-spectral method has been applied to the generic problem of fluid–structure interaction, the flutter instability of a flag in parallel planar flow. Our method allows to use simple Cartesian grids, all information about the time-dependent geometry is contained in the penalization term added to the Navier–Stokes equations. The non-linear coupling has been realized using a fast explicit staggered scheme.

The comparison with the viscous linear stability theory presented in [3] yields favorable agreement. This further confirms the theory, as the numerical simulations in [3] focus mainly on the limit of vanishing bending stiffness, while here we considered a finite value.

Compared with the inviscid model proposed in [18], we also confirm that the flapping frequency is constant and does neither depend on the reduced inflow velocity nor on the Reynolds number. The values obtained for the Strouhal number are comparable with the ones extracted from [18]. The difference of about 10% is related to the use of different approaches. We also focused our attention on a particular set of parameters, which was in [18] found to be chaotic. A direct comparison shows that a finite Reynolds number seems to inhibit the transition to chaos since we do not observe a breakdown of periodicity even for a Reynolds number of 1000.

For the transition from periodic to chaotic fluttering, we reported the observation of a transitional state. In this case the system sustains periodic fluttering during a finite time before passing to irregular oscillations. A time–frequency decomposition, the continuous wavelet transform of the time history of the drag force, is used to illustrate this behavior. The different characteristics of the periodic and chaotic states were pointed out, in particular that the frequencies of displacement, lift and drag are no longer correlated. The chaotic state is also marked by the occurrence of violent intermittent accelerations of the trailing edge. The vortex dynamics of these snapping events have been analyzed, revealing characteristic asymmetric dipoles shed into the wake.

## Acknowledgment

We thankfully acknowledge the DFH-UFA (Deutsch-Französische Hochschule/Université Franco-Allemande) for financial support.

## References

- [1] Kolomenskiy D, Schneider K. A Fourier spectral method for the Navier–Stokes equations with volume penalization for moving solid obstacles. *J Comput Phys* 2009;228:5687–709.
- [2] Michelin S. Falling, flapping, flying, swimming, etc.: high-Re fluid–solid interactions with vortex shedding. PhD thesis, University of California, San Diego; 2009.
- [3] Connell BSH, Yue DKP. Flapping dynamics of a flag in a uniform stream. *J Fluid Mech* 2007;581:33–67.
- [4] Childress S, Hosoi A, Schultz WW, Wang ZJ, editors. Natural locomotion in fluids and on surfaces: swimming, flying and sliding. Springer; 2012.
- [5] Eloy C. Optimal Strouhal number for swimming animals. *J Fluids Struct* 2012;30:205–18.
- [6] Alben S. Optimal flexibility of a flapping appendage in an inviscid fluid. *J Fluid Mech* 2008;614:355–80.
- [7] Ramananarivo S, Godoy-Diana R, Thiria B. Rather than resonance, flapping wing flyers may play on aerodynamics to improve performance. *Proc Natl Acad Sci USA* 2011;108:5964–9.
- [8] Huang L. Flutter of cantilevered plates in axial flow. *J Fluids Struct* 1995;9:127–47.
- [9] Watanabe Y, Suzuki S, Sugihara M, Sueoka Y. An experimental study of paper flutter. *J Fluids Struct* 2002;16:529–42.
- [10] Tang L, Pandoussis MP, Jiang J. Cantilevered flexible plates in axial flow: energy transfer and the concept of flutter-mill. *J Sound Vib* 2009;326:263–76.
- [11] Kuhl J, Desjardin P. Power production locality of bluff body flutter mills using fully coupled 2D direct numerical simulation. *J Fluids Struct* 2012;28:456–72.
- [12] Kornecki A, Dowell E, O'Brien J. On the aeroelastic instability of two-dimensional panels in uniform incompressible flow. *J Sound Vib* 1976;47:163–78.
- [13] Eloy C, Souilliez C, Schouveiler L. Aeroelastic instability of a flexible plate in a uniform flow. *J Fluid Mech* 2008;611:97–106.
- [14] Shelley MJ, Zhang J. Flapping and bending bodies interacting with fluid flows. *Annu Rev Fluid Mech* 2011;43:449–65.
- [15] Pandoussis P. Fluid–structure interactions: slender structures and axial flow. Academic Press; 1998.
- [16] Taneda S. Waving motions of flags. *J Phys Soc Jpn* 1968;24:392–401.
- [17] Shelley M, Vandenberghen N, Zhang J. Heavy flags undergo spontaneous oscillations in flowing water. *Phys Rev Lett* 2005:94.
- [18] Michelin S, Smith SL, Glover B. Vortex shedding model of a flapping flag. *J Fluid Mech* 2008;617:1–10.
- [19] Zhu L, Peskin CS. Simulation of a flapping flexible filament in a flowing soap film by the immersed boundary method. *J Comput Phys* 2002;179:452–68.
- [20] Zhang J, Childress S, Libchaber A, Shelley M. Flexible filaments in a flowing soap film as a model for one-dimensional flags in a two-dimensional wind. *Nature* 2000;408:835–9.
- [21] Sawada T, Hisada T. Fluid–structure interaction analysis of the two-dimensional flag-in-wind problem by an interface-tracking ALE finite element method. *Comput Fluids* 2007;36:136–46.
- [22] Huang W-X, Shin SJ, Sung HJ. Simulation of flexible filaments in a uniform flow by the immersed boundary method. *J Comput Phys* 2007;226:2206–28.
- [23] Balint T, Lucey A. Instability of a cantilevered flexible plate in viscous channel flow. *J Fluids Struct* 2005;20:893–912.
- [24] Farnell DJ, David T, Barton DC. Numerical simulations of a filament in a flowing soap film. *Int J Numer Methods Fluids* 2004;44:313–30.
- [25] Bathe K, Zhang H. A mesh adaptivity procedure for CFD and fluid–structure interactions. *Comput Struct* 2009;87:604–17.
- [26] Slone A, Pericleous K, Bailey C, Cross M. Dynamic fluid–structure interaction using finite volume unstructured mesh procedures. *Comput Struct* 2002;80:371–90.
- [27] Bathe K, Zhang H. A flow-condition-based interpolation finite element procedure for incompressible fluid flows. *Comput Struct* 2002;80:1267–77.
- [28] Mittal R, Iaccarino G. Immersed boundary methods. *Annu Rev Fluid Mech* 2005;37:239–61.
- [29] Peskin CS. The immersed boundary method. *Acta Numer* 2002;11:479–517.
- [30] Arquis E, Caltagirone J-P. Sur les conditions hydrodynamiques au voisinage d'une interface milieu fluide milieu poreux: application à la convection naturelle. *CR Acad Sci Paris Sér II* 1984:299.
- [31] Angot P, Bruneau C, Fabrie P. A penalization method to take into account obstacles in incompressible viscous flows. *Numer Math* 1999;81:497–520.
- [32] Carbow G, Fabrie P. Boundary layer for a penalization method for viscous incompressible flow. *Adv Differ Equ* 2003;8:1453–2480.
- [33] Schneider K. Numerical simulation of the transient flow behaviour in chemical reactors using a penalisation method. *Comput Fluids* 2005;34:1223–38.
- [34] Schneider K, Farge M. Numerical simulation of the transient flow behaviour in tube bundles using a volume penalization method. *J Fluids Struct* 2005;20:555–66.
- [35] Keetels G, D'Ortona U, Kramer W, Clercx H, Schneider K, van Heijst G. Fourier spectral and wavelet solvers for the incompressible Navier–Stokes equations with volume-penalization: convergence of a dipole-wall collision. *J Comput Phys* 2007;227:919–45.
- [36] Nguyen van yen R, Kolomenskiy D, Schneider K. Approximation of the Laplace and Stokes operators with Dirichlet boundary conditions through volume penalization: a spectral viewpoint. *ArXiv e-prints*, 2012. <arXiv:1206.0002>.

- [37] Uhlmann M. An immersed boundary method with direct forcing for the simulation of particulate flows. *J Comput Phys* 2005;209:448–76.
- [38] Canuto C, Hussaini MY, Quarteroni A, Zang TA. Spectral methods – evolution to complex geometries and applications to fluid dynamics. Springer; 2007.
- [39] Schenk O, Gsrtner K. Solving unsymmetric sparse systems of linear equations with PARDISO. *Future Gener Comput Syst* 2004;20:475–87.
- [40] Foerster C, Wall W, Ramm E. Artificial added mass instabilities in sequential staggered coupling of nonlinear structures and incompressible viscous flows. *Comput Methods Appl Mech Eng* 2007;196:1278–93.
- [41] Turek S, Hron J. Proposal for numerical benchmarking of fluid–structure interaction between an elastic object and laminar incompressible flow. In: Bungartz H, Schäfer M, editors. Fluid–structure interaction: modelling, simulation, optimisation. Lecture notes in computational science and engineering, vol. 53. Berlin, Heidelberg: Springer; 2006. p. 371–85.
- [42] Farge M, Schneider K. Wavelets: application to turbulence. In: Françoise J-P, Naber GL, Tsun TS, editors. Encyclopedia of mathematical physics. Oxford: Academic Press; 2006. p. 408–20.